electronics

MDPI

Article

Low-Resolution Optimization for an Unmanned Aerial Vehicle Communication Network Under a Passive Reconfigurable Intelligent Surface and Active Reconfigurable Intelligent Surface

Qiangqiang Yang [1,2], Yufeng Chen [1], Zhiyu Huang [1], Hongwen Yu [1] and Yong Fang [1,*]

[1] School of Communication and Information Engineering, Shanghai University, Shanghai 200444, China; yangqq@shu.edu.cn (Q.Y.); cyf119@shu.edu.cn (Y.C.); rain-huang@shu.edu.cn (Z.H.); hw_yu@shu.edu.cn (H.Y.)
[2] School of Electronics and Information Engineering, Shanghai University of Electric Power, Shanghai 200444, China
* Correspondence: yfang@shu.edu.cn

Abstract: This paper investigates the optimization of an unmanned aerial vehicle (UAV) network serving multiple downlink users equipped with single antennas. The network is enhanced by the deployment of either a passive reconfigurable intelligent surface (RIS) or an active RIS. The objective is to jointly design the UAV's trajectory and the low-bit, quantized, RIS-programmable coefficients to maximize the minimum user rate in a multi-user scenario. To address this optimization challenge, an alternating optimization framework is employed, leveraging the successive convex approximation (SCA) method. Specifically, for the UAV trajectory design, the original non-convex optimization problem is reformulated into an equivalent convex problem through the introduction of slack variables and appropriate approximations. On the other hand, for the RIS-programmable coefficient design, an efficient algorithm is developed using a penalty-based approximation approach. To solve the problems with the proposed optimization, high-performance optimization tools such as CVX are utilized, despite their associated high time complexity. To mitigate this complexity, a low-complexity algorithm is specifically tailored for the optimization of passive RIS-programmable reflecting elements. This algorithm relies solely on closed-form expressions to generate improved feasible points, thereby reducing the computational burden while maintaining reasonable performance. Extensive simulations are created to validate the performance of the proposed algorithms. The results demonstrate that the active RIS-based approach outperforms the passive RIS-based approach. Additionally, for the passive RIS-based algorithms, the low-complexity variant achieves a reduced time complexity with a moderate loss in performance.

Keywords: reconfigurable intelligent surface (RIS); unmanned aerial vehicle (UAV) networks; successive convex approximation (SCA); low-bit quantized programmable coefficients

Citation: Yang, Q.; Chen, Y.; Huang, Z.; Yu, H.; Fang, Y. Low-Resolution Optimization for an Unmanned Aerial Vehicle Communication Network Under a Passive Reconfigurable Intelligent Surface and Active Reconfigurable Intelligent Surface. *Electronics* **2024**, *13*, 1826. https://doi.org/10.3390/electronics13101826

Academic Editors: Yung-Fa Huang and Christos J. Bouras

Received: 9 April 2024
Revised: 30 April 2024
Accepted: 3 May 2024
Published: 8 May 2024

1. Introduction

The future of 5G radio access networks promises to revolutionize connectivity, supporting unprecedented traffic volumes, billions of connected devices, and diverse requirements regarding reliability, latency, and battery life [1]. However, with the explosive growth of mobile data traffic driven by the Internet of Things, the global mobile traffic is expected to hit 1 zettabyte per month by 2028, placing immense strain on current infrastructure and telecom operators. While HetNets have been explored to address this challenge, unexpected or emergency situations often render the deployment of terrestrial infrastructure economically unviable. In such scenarios, intelligent heterogeneous architecture utilizing Unmanned Aerial Vehicles (UAVs) emerges as a promising solution [2]. UAVs offer a cost-effective and adaptable approach to facilitate key usage scenarios like enhanced Mobile Broadband

(eMBB), Ultra-Reliable Low-Latency Communications (URLLC), and massive Machine-Type Communications (mMTC). Their potential to provide network service recovery in disasters, enhance public safety, and handle emergencies underscores the importance of UAVs as a crucial component of 5G/B5G wireless technologies [3]. With the ever-evolving landscape of wireless communication, UAVs have become indispensible components of the quest to move beyond fifth-generation networks. As technology marches forward, these aerial vehicles have established themselves as pivotal players, revolutionizing the field with their unparalleled capabilities [4]. Distinguishing themselves from traditional ground-based stations, UAVs offer unique benefits, such as superior mobility, cost-effectiveness, and unhindered line-of-sight transmission. These advantages have led to the extensive utilization of UAVs in diverse fields, leveraging their versatility and high mobility for a wide range of applications [5]. From the perspective of wireless communication, UAVs can be deployed as aerial communication platforms, for instance, as flying base stations or mobile relays. By mounting communication transceivers, UAVs can provide or enhance communication services to ground targets in high-traffic and overloaded scenarios; these are commonly referred to as UAV-assisted communications. Additionally, UAVs can function as aerial nodes, enabling a multitude of applications ranging from cargo delivery to surveillance; these are known as cellular-connected UAVs [6]. While UAVs offer numerous innovative opportunities for wireless communication, the deployment of ground infrastructure in emergency or unexpected situations often faces economic and environmental challenges. In this context, the potential and value of UAVs as an integral part of 5G/B5G wireless technology become even more evident. As we continue to explore the boundaries of wireless communication, UAVs will undoubtedly play a crucial role in shaping the future of our connected world.

Leveraging these attributes, UAVs can serve as temporary airborne base stations, significantly improving communication quality for terrestrial users. To optimize the UAV communication network and achieve the maximal rate or energy efficiency, research has focused on trajectory and placement optimization [7–9]. Ref. [7] proposed a mobile relaying technique using UAVs, demonstrating that, by optimizing the source/relay transmit power and relay trajectory under practical constraints, significant throughput gains can be achieved compared to static relaying, thus highlighting the potential of UAV-based mobile relaying for performance enhancement. Energy-efficient wireless communication with unmanned aerial vehicles were investigated in [8] by optimizing their horizontal trajectory at a fixed altitude, considering both communication throughput and propulsion energy consumption. Ref. [9] explored energy minimization in a UAV-assisted sensor network by jointly optimizing the UAV trajectory and sensor uploading power, utilizing a TSP-based approach for optimal serving orders and a PSPSCA/AQSCA algorithm for UAV positioning and sensor power allocation, achieving a superior performance compared to benchmark schemes. This strategic endeavor aims to meticulously shape the UAV's trajectory, thereby enhancing the network's user rate or energy efficiency [10–12]. Ref. [10] investigated a UAV-enabled multicasting system, optimizing the UAV trajectory to minimize mission time and ensure high-probability file recovery. A fly-and-communicate protocol for minimizing completion time and energy consumption in UAV-enabled multicasting was designed in [11]. For quadrotor UAVs within the IoT framework, an optimized energy consumption model is established in [12].

Despite the significant potential of unmanned aerial vehicles (UAVs) to enhance communication quality by optimizing their trajectory or placement, the intricate landscapes of air-to-ground (A2G) communications introduce a set of unique challenges. One such challenge is the potential for link blockage in complex environments [13,14]. The presence of obstacles like tall buildings, mountains, and dense foliage can cause signal interference and attenuation, resulting in a significant reduction in communication quality. This issue becomes even more critical in urban areas, where the dense concentration of buildings and other structures can create numerous obstacles for A2G links. To address this challenge, researchers have explored various techniques to optimize the trajectory and placement

of UAVs [15]. For instance, by leveraging advanced algorithms and models, UAVs can be directed to avoid areas with high potential for link blockage. Additionally, the use of multiple UAVs in a coordinated manner can help ensure redundancy and reliability in communication links, minimizing the impact of link blockage on overall network performance [16]. However, the successful implementation of these techniques requires a deep understanding of the intricacies of A2G communication landscapes. Factors such as the density and distribution of obstacles, the propagation characteristics of radio waves, and the dynamic nature of the environment must all be taken into account. By considering these factors and developing innovative solutions, we can harness the full potential of UAVs to enhance communication quality, even in the most complex and challenging environments. To surmount this hurdle, certain researchers have turned to reconfigurable intelligent surfacs (RIS) [17–19]. Ref. [17] introduced the integration of wireless localization and sensing capabilities, tailored for future cellular systems, where, by manipulating electromagnetic characteristics, RISs' performance can be enhanced, opening new research horizons. Overviews of future communications are provided in [18,19], including the available hardware architectures for reconfiguring such surfaces and highlighting the related opportunities. By integrating an RIS into multi-user wireless communication networks featuring UAV deployments, the quality of A2G communication links can be elevated through the intelligent configuration of the RIS components [20–24]. Guided by the aforementioned advantages of integrating RIS into UAV-assisted wireless networks, several prior studies have endeavored to explore the potential performance enhancements brought forth by RIS in a range of scenarios pertaining to UAV-based air-to-ground communication [25–28]. In the study presented by [25], UAVs and RISs were employed to enhance communications by jointly optimizing the UAV's trajectory, phase shifts of the RIS, allocation of sub-bands, and power control to maximize the minimum average achievable rate for all ground users (GUs) in the system. To maximize the system rate performance, the conjugate gradient and particle swarm optimization scheme was proposed to optimize the RIS phase shifts and the UAV altitudes [26]. A communication system involving a UAV and an RIS for ground-based IoT devices was investigated in [27], where the performance of the network was enhanced by optimizing the UAV's placement and beamforming of RIS. An RIS was employed to enhance the communication quality of UAV-based communication systems [28], an alternating optimization technique that optimized the UAV trajectory and RIS beamforming to maximize the average communication rate was proposed.

The investigation into active RIS and passive RIS has yielded profound insights into their respective roles in enhancing multiuser communication within UAV networks [29]. Passive RIS, with its fixed phase shifts, offers a cost-effective solution for improving signal reception without the need for additional power amplification. Its simplicity and reliability make it a viable option in various communication scenarios. However, the lack of active interference management limits its performance in complex environments [30]. On the other hand, active RIS, with its tunable phase shifts and amplification capabilities, offers greater flexibility and performance enhancements [31,32]. Its ability to actively manage interference and optimize signal transmission opens up new possibilities for enhancing communication efficiency and reliability. While the added complexity and cost may be a consideration, the significant improvements in communication performance justify its use in critical applications [33,34].

The above investigations have studied unquantized, programmable RIS coefficients' optimization in RIS-assisted UAV networks. In this paper, quantized programmable RIS coefficients' optimization is investigated, and the main contribution of this work can be summarized as follows:

- The study focuses on passive, RIS-assisted, multi-user communication within UAV communication networks, aiming to maximize users' worst rate. To efficiently solve this optimization problem, it is decomposed into two subproblems: trajectory design and PREs optimization. The SCA method is used to convexify the subproblems, and a two-stage algorithm with high complexity is proposed to alternately optimize them.

To simplify the algorithm, a closed-form solution is derived for the phase optimization subproblem within passive RIS settings.

- To further enhance the benefits of RIS, this study explores active RIS (aRIS)-assisted multiuser communication within a UAV communication system. Distinguishing from passive RIS, the aRIS-assisted UAV network experiences self-interference. To address this, a two-stage algorithm is proposed, incorporating power-amplified PREs optimization and UAV trajectory design.

Notation. Variables are printed in boldface; A^H denotes the Hermitian conjugate of matrix A. For a vector $x = (x_1, \ldots, x_n)^T$, $\mathrm{Diag}(x)$ creates a diagonal matrix with x as its diagonal entries. $[A]^2$ corresponds to AA^H, $\langle A \rangle$ signifies the trace of matrix A, and $\langle A, B \rangle$ is the trace of $A^H B$, applicable to matrices A and B. The Frobenius norm of matrix A is defined as $||A|| = \sqrt{\mathrm{trace}(A^H A)}$, which is also equal to $\sqrt{\sum_{i=1}^{m} \sum_{j=1}^{n} a_{ij}^2}$. $A \succeq 0$ ($A \succ 0$) signifies that A is a positive semi-definite (positive definite) matrix. $\lambda_{\max}(A)$ represents the largest eigenvalue of the Hermitian symmetric matrix A. A circular Gaussian random variable with a zero mean and variance σ is represented as $\mathcal{C}(0, \sigma)$.

2. Problem Statements and Reformulations

Consider the downlink transmission of an RIS-assisted UAV communication network, as shown in Figure 1, where the direct links between the UAV and users are blocked by obstacles. An RIS is deployed at a high altitude to guarantee line-of-sight communication with K single-antenna users, as indicated in [35]. The UAV is equipped with a single antenna and the flight time of T is equally divided into the N time slot with the slot lenth δ_t. We assume that the horizontal locations of RIS and GUs are denoted by $\boldsymbol{w}_r = [x_r, y_r, z_r]^T$ and $\boldsymbol{w}_k = [x_k, y_k, 0]^T$, respectively, with $k \in \mathcal{K} \triangleq \{1, \ldots, K\}$. The UAV's trajectory can be approximated by the sequence $\boldsymbol{q}_n = [x_n, y_n, z]^T$, $n \in \mathcal{N} \triangleq \{1, \ldots, N\}$, with the following constraints:

$$\|\boldsymbol{q}_n - \boldsymbol{q}_{n-1}\| \leq V_{max}\delta_t, \forall n, \tag{1}$$

$$\boldsymbol{q}_{ini} = \boldsymbol{q}_0, \boldsymbol{q}_{end} = \boldsymbol{q}_N, \tag{2}$$

where $\boldsymbol{q}_{ini}$ and $\boldsymbol{q}_{end}$ denote the initial point and end point of the UAV, respectively.

The RIS is equipped with $M = M_x \times M_z$ elements, forming an $M_x \times M_z$ uniform rectangular array. Let $\mathbf{z}_n \triangleq (\mathbf{z}_{n,1}, \ldots, \mathbf{z}_{n,M})^T$ denote the programmable coefficients of the mth-reflecting element in the nth time slot.

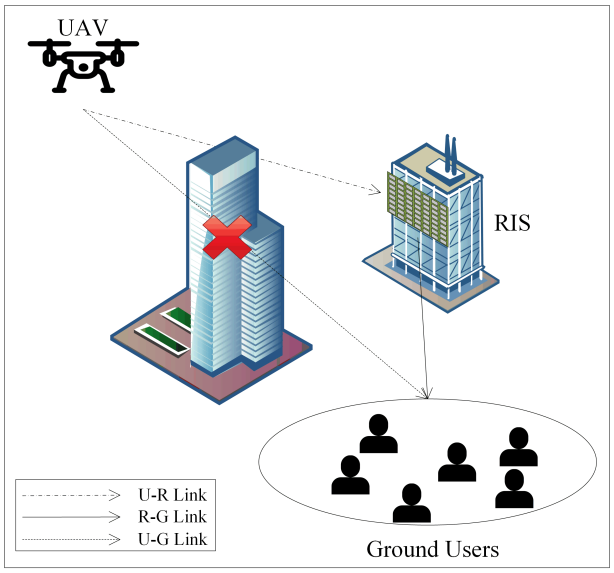

Figure 1. RIS-assisted multi-user communication network.

Let $\tilde{h}_{\mathrm{n,R\text{-}k}} = \sqrt{\beta_{\mathrm{n,RIS\text{-}k}}} h_{\mathrm{n,R\text{-}k}} \in \mathbb{C}^{M\times 1}$ and $\tilde{G}_{\mathrm{n,U\text{-}R}} = \sqrt{\beta_{\mathrm{n,UAV\text{-}RIS}}(\boldsymbol{q}_n)} G_{\mathrm{U\text{-}R,n}} \in \mathbb{C}^{1\times M}$ denote the baseband equivalent channels for the RIS→user k, UAV→user k links in the nth time slot, respectively, with $k \in \mathcal{K} \triangleq \{1,\ldots,K\}$, $\beta_{\mathrm{n,RIS\text{-}k}} = \beta_0 d_{k,Rk}^{-\alpha}$ and $\beta_{\mathrm{n,UAV\text{-}RIS}} = \beta_0 d_{n,UR}^{-\kappa}$. β_0 is the path loss at the reference distance, α and κ are the path loss exponents related to the RIS-to-GUs (R-G) link and UAV-to-RIS (U-R) link, and $d_{n,Rk}$ and $d_{n,UR}(\boldsymbol{q}_n)$ are the distance between the RIS and kth ground user and the distance between the UAV and the RIS during the nth slot, respectively [36–38]. $h_{\mathrm{n,R\text{-}k}}$ and $G_{\mathrm{n,U\text{-}R}}$ are modeled by Rician fading, presenting the RIS→user k and UAV→RIS links in the nth time slot, respectively [36].

2.1. Passive RIS

Like many other papers on RIS-assisted UAV communication networks [14–16], the effective channel spanning from the UAV to user k assisted by passive RIS in the nth time slot is given by the following:

$$\begin{aligned}\tilde{\mathcal{H}}_{n,k}(\mathbf{q}_n,\mathbf{z}_n) &= \tilde{h}_{\mathrm{n,R\text{-}k}} R_{\mathrm{R\text{-}k}}^{1/2} \mathsf{diag}(\mathbf{z}_\mathsf{n}) \tilde{\mathsf{G}}_{\mathrm{n,U\text{-}R}}(\mathbf{q}_\mathsf{n}) \\ &= \sqrt{\beta_{\mathrm{n,RIS\text{-}k}}} h_{\mathrm{n,R\text{-}k}} R_{\mathrm{R\text{-}k}}^{1/2} \mathsf{diag}(\mathbf{z}_\mathsf{n}) \sqrt{\mathsf{fi}_{\mathrm{n,UAV\text{-}RIS}}(\mathbf{q}_\mathsf{n})} \mathsf{G}_{\mathrm{n,U\text{-}R}}(\mathbf{q}_\mathsf{n}) \\ &= \tilde{h}_{\mathrm{n,R\text{-}}k} \mathsf{diag}(\mathbf{z}_\mathsf{n}) \mathsf{G}_{\mathrm{n,U\text{-}R}}(\mathbf{q}_\mathsf{n}) \in \mathbb{C}^{1\times \mathsf{M}}. \end{aligned} \tag{3}$$

for

$$\tilde{h}_{\mathrm{n,R\text{-}k}} \triangleq \sqrt{\beta_{\mathrm{n,UAV\text{-}RIS}}(\boldsymbol{q}_n)} \sqrt{\beta_{\mathrm{n,RIS\text{-}k}}} h_{\mathrm{n,R\text{-}k}} R_{\mathrm{R\text{-}k}}^{1/2}, \tag{4}$$

where $R_{\mathrm{R\text{-}k}} \in \mathbb{C}^{M\times M}$ represents the spatial correlation matrix of RIS's PREs with respect to user k [37,39].

We consider PREs with b-bit resolution, which leads to

$$\mathbf{z}_{n,m} = e^{j\boldsymbol{\theta}_{n,m}}, m \in \mathcal{M}, \tag{5}$$

with

$$\boldsymbol{\theta}_{n,m} \in \Delta \triangleq \left\{ \alpha \frac{2\pi}{2^b}, \alpha = 0,1,\ldots,2^b-1 \right\}, m \in \mathcal{M}. \tag{6}$$

Let $s_k \in \mathcal{C}(0,1)$ with $\mathbb{E}(|s_k|^2) = 1$ represent the information intended for user k, and let P_k be the split power for user k transmitted by the UAV. The signal received from the UAV at user k in the nth time slot can be written as follows:

$$y_{n,k} = \tilde{\mathcal{H}}_{k,n}(\mathbf{q}_n,\mathbf{z}_n) P_k s_k + n_k, \tag{7}$$

where $n_k \in \mathcal{C}(0,\sigma)$ represents the additive white Gaussian noise.

The rate of user k in the nth time slot is expressed as follows:

$$r_{n,k}(\mathbf{q}_n,\mathbf{z}_n) = \ln\left(1 + \frac{|\tilde{\mathcal{H}}_{n,k}(\mathbf{q}_n,\mathbf{z}_n)\sqrt{P_k}|^2}{\sum_{j\in\mathcal{K}\setminus\{k\}} |\tilde{\mathcal{H}}_{n,k}(\mathbf{q}_n,\mathbf{z}_n)\sqrt{P_j}|^2 + \sigma}\right), k \in \mathcal{K}. \tag{8}$$

The max–min rate optimization problem (MR problem) can be expressed as follows:

$$\max_{\mathbf{z}_n,\mathbf{q}_n} \min_{k\in\mathcal{K}} r_{n,k}(\mathbf{q}_n,\mathbf{z}_n) \quad \text{s.t.} \quad (1),(2),(5),(6), \tag{9}$$

To solve the MR problem (9), we alternately optimize the UAV trajectory and RIS PREs. Specifically, for $r_{n,k}(\mathbf{z}_n) \triangleq [r_{n,1}(\mathbf{q}_n,\mathbf{z}_n),\ldots,r_{n,K}(\mathbf{q}_n,\mathbf{z}_n)]^T \in \mathbb{R}^K$, the MR problem is given by

$$\max_{\mathbf{q}_n,\mathbf{z}_n\boldsymbol{\theta}_n} f_p[r_n(\mathbf{q}_n,\mathbf{z}_n)] \triangleq \min_{k\in\mathcal{K}} r_{n,k}(\mathbf{q}_n,\mathbf{z}_n) \quad \text{s.t} \quad (1),(2),(5),(6). \tag{10}$$

We use the penalty term $||\mathbf{z}_n - e^{j\boldsymbol{\theta}_n}||^2$ to eliminate the discrete constraints (5), leading to the following exactly penalized optimization problem:

$$\max_{\mathbf{q}_n,\mathbf{z}_n,\boldsymbol{\theta}_n} f_{p,c}(\mathbf{q}_n,\mathbf{z}_n,\boldsymbol{\theta}_n) \triangleq f_p[r_n(\mathbf{q}_n,\mathbf{z}_n)] - c||\mathbf{z}_n - e^{j\boldsymbol{\theta}_n}||^2 \quad \text{s.t.} \quad (1),(2),(6), \tag{11}$$

where $c > 0$ serves as the penalty parameter.

2.2. Active RIS

The effective channel spanning from the UAV to user k assisted by the aRIS in the nth time slot is given by the following:

$$\tilde{\tilde{\mathcal{H}}}_{n,k}(\bar{\mathbf{q}}_n,\bar{\mathbf{z}}_n) = \tilde{h}_{\text{n,aR-k}}\text{diag}(\bar{\mathbf{z}}_n)G_{\text{n,U-aR}}(\bar{\mathbf{q}}_n) \in \mathbb{C}^{1\times M}. \tag{12}$$

For the practical implementation of aRIS, we consider power-amplified PREs with a b-bit resolution, which leads to the following:

$$\bar{\mathbf{z}}_{n,m} = \boldsymbol{p}_{n,m}e^{j\bar{\boldsymbol{\theta}}_{n,m}}, m \in \mathcal{M}, \tag{13}$$

with $\boldsymbol{p}_{n,m} \in \mathbb{R}$ defining the power amplification coefficients, and

$$\bar{\boldsymbol{\theta}}_{n,m} \in \Lambda \triangleq \left\{\beta\frac{2\pi}{2^b}, \beta = 0,1,\ldots,2^b-1\right\}, m \in \mathcal{M}. \tag{14}$$

defining the PREs of b-bit resolution.

The signal received from the UAV at user k in the nth time slot can be written as follows:

$$\bar{y}_{n,k} = \tilde{\tilde{\mathcal{H}}}_{n,k}(\mathbf{z}_n,\boldsymbol{q}_n)P_k s_k + \tilde{h}_{\text{n,R-k}}\text{diag}[\bar{\mathbf{z}}_{n,m}]_{m\in\mathcal{M}}\nu + n_k, \tag{15}$$

where $\nu \in \mathcal{C}(0,\sigma_\nu I)$ is the dynamic noise induced by aRIS.

The rate of user k in the nth time slot is expressed as follows:

$$\bar{r}_{n,k}(\bar{\mathbf{q}}_n,\bar{\mathbf{z}}_n) = \ln\left(1 + \frac{|\tilde{\tilde{\mathcal{H}}}_{n,k}(\bar{\mathbf{q}}_n,\bar{\mathbf{z}}_n)\sqrt{P_k}|^2}{\sum_{j\in\mathcal{K}\setminus\{k\}}|\tilde{\tilde{\mathcal{H}}}_{n,k}(\bar{\mathbf{q}}_n,\bar{\mathbf{z}}_n)\sqrt{P_j}|^2 + \sigma_\nu\sum_{m\in\mathcal{M}}|\tilde{h}_{\text{n,R-k}}(m)|^2|\bar{\mathbf{z}}_{n,m}|^2 + \sigma}\right), \quad k \in \mathcal{K}. \tag{16}$$

The reflected power constraint of the aRIS given the budget P_A is as follows:

$$\sum_{k\in\mathcal{K}}||\text{diag}[\bar{\mathbf{z}}_{n,m}]_{m\in\mathcal{M}}G_{n,U-R}(\bar{\mathbf{q}}_n)||^2P_k + \sigma_\nu||\text{diag}[\bar{\mathbf{z}}_{n,m}]_{m\in\mathcal{M}}||^2 \le P_A \tag{17}$$

$$\Leftrightarrow \quad \bar{\mathbf{z}}_n^H\mathcal{Q}_1\bar{\mathbf{z}}_n \le P_A, \tag{18}$$

where

$$\mathcal{Q}_1 \triangleq \textstyle\sum_{k\in\mathcal{K}}\text{diag}[|G_{n,U-R}(\bar{\mathbf{q}}_n)|^2P_k]_{m\in\mathcal{M}} + \sigma_\nu I_M. \tag{19}$$

The MR problem can be formulated as follows:

$$\max_{\mathbf{z}_n,\mathbf{q}_n}\min_{k\in\mathcal{K}}\bar{r}_{n,k}(\bar{\mathbf{q}}_n,\bar{\mathbf{z}}_n) \quad \text{s.t.} \quad (1),(2),(13),(14),(18). \tag{20}$$

Similarly, for $\bar{r}_n(\bar{\mathbf{q}}_n,\bar{\mathbf{z}}_n) \triangleq [\bar{r}_{n,1}(\bar{\mathbf{q}}_n,\bar{\mathbf{z}}_n),\ldots,\bar{r}_{n,K}(\bar{\mathbf{q}}_n,\bar{\mathbf{z}}_n)]^T \in \mathbb{R}^K$, the MR problem is written as follows:

$$\max_{\bar{\mathbf{q}}_n,\bar{\mathbf{z}}_n,\bar{\boldsymbol{\theta}}_n}\bar{f}_a[\bar{r}_n(\bar{\mathbf{q}}_n,\bar{\mathbf{z}}_n)] \triangleq \min_{k\in\mathcal{K}}\bar{r}_{n,k}(\bar{\mathbf{q}}_n,\bar{\mathbf{z}}_n) \quad \text{s.t} \quad (1),(2),(13),(14),(18). \tag{21}$$

We use the penalty term $|\bar{\mathbf{z}}_{n,m} - \boldsymbol{p}_{n,m}e^{j\bar{\boldsymbol{\theta}}_{n,m}}|^2$ to eliminate the discrete constraints (13), leading to the following exactly penalized optimization problem:

$$\max_{\bar{\mathbf{q}}_n,\bar{\mathbf{z}}_n,\boldsymbol{p}_n,\bar{\boldsymbol{\theta}}_n} \bar{f}_{a,\rho}(\bar{\mathbf{q}}_n,\bar{\mathbf{z}}_n,\boldsymbol{p}_n,\bar{\boldsymbol{\theta}}_n) \triangleq \bar{f}_a[\bar{r}_n(\bar{\mathbf{q}}_n,\bar{\mathbf{z}}_n)] - \rho \sum_{m\in\mathcal{M}} |\bar{\mathbf{z}}_{n,m} - \boldsymbol{p}_{n,m}e^{j\bar{\boldsymbol{\theta}}_{n,m}}|^2$$
$$\text{s.t.} \quad (1), (2), (14), (18). \tag{22}$$

where $\rho > 0$ serves as the penalty parameter.

3. Passive RIS Convex-Solver-Based Algorithms

Alternating optimization is studied in this part with respect to each of the variables $(\mathbf{q}_n, \mathbf{z}_n, \boldsymbol{\theta}_n)$ while holding the others fixed to generate the next iterative point. Starting with the initialization of (11) using the feasible point $(q_n^{(0)}, z_n^{(0)}, \theta_n^{(0)})$, let $(q_n^{(\tau)}, z_n^{(\tau)}, \theta_n^{(\tau)})$ denote a feasible point for (11) obtained from the $(\tau-1)$-st iteration.

3.1. Alternating Optimization of UAV Trajectory

To seek $q_n^{(\tau)}$ so that

$$f_p[q_n^{(\tau+1)}, z_n^{(\tau)}, \theta_n^{(\tau)}] > f_p[q_n^{(\tau)}, z_n^{(\tau)}, \theta_n^{(\tau)}], \tag{23}$$

the trajectory optimization subproblem can be reformulated as follows:

$$\max_{\mathbf{q}_n} \min_k \quad \frac{1}{N}\sum_{n=1}^{N} \ln\left(1 + \frac{|\tilde{\mathcal{H}}_{n,k}(\mathbf{q}_n)|^2 P_k}{\sum_{j\in\mathcal{K}\setminus\{k\}} |\tilde{\mathcal{H}}_{n,k}(\mathbf{q}_n)|^2 P_j + \sigma}\right) \tag{24a}$$
$$\text{s.t.} \quad (1) - (2). \tag{24b}$$

By introducing the slack variable s, problem (24) can be given by

$$\max_{\mathbf{q}_n, s} \quad s \tag{25a}$$
$$\text{s.t.} \quad (1)\text{–}(2), \tag{25b}$$
$$\frac{1}{N}\sum_{n=1}^{N} \ln\left(1 + \frac{A_{n,k}^{(\tau)}}{B_{n,k}^{(\tau)} + d_{n,U-R}^{\kappa}(\mathbf{q}_n)}\right) \geq s, \forall k \in \mathcal{K}. \tag{25c}$$

where $A_{n,k}^{(\tau)} = |\tilde{h}_{\text{n,R-k}}\text{diag}(\mathbf{z}_n^{\tau})\sqrt{\beta_0}G_{\text{U-R,n}}|^2 P_k/\sigma$, $B_{n,k}^{(\tau)} = \sum_{j\in\mathcal{K}\setminus\{k\}} |\tilde{h}_{\text{n,R-j}}\text{diag}(\mathbf{z}_n^{\tau})\sqrt{\beta_0}G_{\text{U-R,n}}|^2 P_j/\sigma$ and $d_{n,U-R}^{\kappa}(\mathbf{q}_n) = \|\boldsymbol{q}_n - \boldsymbol{w}_r\|^{\kappa}$.

However, the problem (25a) cannot be solved directly due to the nonconvex constraint (25c). By using the inequality (A1), the lower bound of the left-hand side of the constraint (25c) can be derived at the feasible point $\boldsymbol{q}_n^{\tau}$:

$$\begin{aligned}\frac{1}{N}\sum_{n=1}^{N} \ln\left(1 + \frac{A_{n,k}^{(\tau)}}{B_{n,k}^{(\tau)} + d_{n,U-R}^{\kappa}(\mathbf{q}_n)}\right) &\geq \frac{1}{N}\sum_{n=1}^{N} \ln\left(1 + \frac{A_{n,k}^{(\tau)}}{B_{n,k}^{(\tau)} + d_{n,U-R}^{r,\kappa}}\right) \\ &+ \frac{A_{n,k}^{(\tau)}}{A_{n,k}^{(\tau)} + B_{n,k}^{(\tau)} + d_{n,U-R}^{(\tau)\kappa}}\left(1 - \frac{d_{n,U-R}^{\kappa}}{d_{n,U-R}^{(\tau)\kappa}}\right) \\ &\triangleq \bar{R}_k^{lb},\end{aligned} \tag{26}$$

Thus, the trajectory optimization problem can be expressed as follows:

$$\max_{\boldsymbol{q}_n, s} \quad s \tag{27a}$$
$$\text{s.t.} \quad (1)\text{–}(2), \tag{27b}$$
$$\bar{R}_k^{lb} \geq s, \forall k \in \mathcal{K}. \tag{27c}$$

3.2. Alternating Optimization of the Passive PREs

To seek $z_n^{(\tau+1)}$, so that:

$$f_{p,c}[q_n^{(\tau+1)}, z_n^{(\tau+1)}, \theta_n^{(\tau)}] > f_{p,c}[q_n^{(\tau+1)}, z_n^{(\tau)}, \theta_n^{(\tau)}] \tag{28}$$

$$\Leftrightarrow \quad f_p[r_n(q_n^{(\tau+1)}, z_n^{(\tau+1)})] - c||z_n^{(\tau)} - e^{j\theta_n^{(\tau)}}||^2 > f_p[r_n(q_n^{(\tau+1)}, z_n^{(\tau)})] - c||z_n^{(\tau)} - e^{j\theta_n^{(\tau)}}||^2, \tag{29}$$

we consider the following problem:

$$\max_{\mathbf{z}_n} \min_{k\in\mathcal{K}} r_{n,k}(\mathbf{z}_n) - c||\mathbf{z}_n - e^{j\theta_n^{(\tau)}}||^2 \tag{30}$$

where, according to (8), we have:

$$r_{n,k}(\mathbf{z}_n) = \ln\left(1 + \frac{|\tilde{\mathcal{H}}_{n,k}(\mathbf{z}_n)\sqrt{P_k}|^2}{\sum_{j\in\mathcal{K}\setminus\{k\}} |\tilde{\mathcal{H}}_{n,k}(\mathbf{z}_n)\sqrt{P_j}|^2 + \sigma}\right), k \in \mathcal{K}. \tag{31}$$

Using the inequality (A2) for $(\boldsymbol{a}, \boldsymbol{b}) = (\tilde{\mathcal{H}}_{n,k}(\mathbf{z}_n)\sqrt{P_k}, \sum_{j\in\mathcal{K}\setminus\{k\}} |\tilde{\mathcal{H}}_{n,k}(\mathbf{z}_n)\sqrt{P_j}|^2)$ and $(\bar{a}, \bar{b}) = (\tilde{\mathcal{H}}_{n,k}(q_n^{(\tau+1)}, z_n^{(\tau)})\sqrt{P_k}, \sum_{j\in\mathcal{K}\setminus\{k\}} |\tilde{\mathcal{H}}_{n,k}(q_n^{(\tau+1)}, z_n^{(\tau)})\sqrt{P_j}|^2)$, we can obtain a concave quadratic function by approximating $r_{n,k}(\mathbf{z}_n)$.

$$\begin{aligned}
\tilde{r}_{1n,k}^{(\tau)}(\mathbf{z}_n) \quad \triangleq \quad & \ln(1 + \frac{|\tilde{\mathcal{H}}_{n,k}(q_n^{(\tau+1)}, z_n^{(\tau)})\sqrt{P_k}|^2}{\sum_{j\in\mathcal{K}\setminus\{k\}} |\tilde{\mathcal{H}}_{n,k}(q_n^{(\tau+1)}, z_n^{(\tau)})\sqrt{P_j}|^2 + \sigma}) \\
& - \frac{|\tilde{\mathcal{H}}_{n,k}(q_n^{(\tau+1)}, z_n^{(\tau)})\sqrt{P_k}|^2}{\sum_{j\in\mathcal{K}\setminus\{k\}} |\tilde{\mathcal{H}}_{n,k}(q_n^{(\tau+1)}, z_n^{(\tau)})\sqrt{P_j}|^2 + \sigma} \\
& - \sigma \frac{|\tilde{\mathcal{H}}_{n,k}(q_n^{(\tau+1)}, z_n^{(\tau)})\sqrt{P_k}|^2}{(\sum_{j\in\mathcal{K}\setminus\{k\}} |\tilde{\mathcal{H}}_{n,k}(q_n^{(\tau+1)}, z_n^{(\tau)})\sqrt{P_j}|^2 + \sigma)(\sum_{j\in\mathcal{K}} |\tilde{\mathcal{H}}_{n,k}(q_n^{(\tau+1)}, z_n^{(\tau)})\sqrt{P_j}|^2 + \sigma)} \\
& + \frac{2}{\sum_{j\in\mathcal{K}\setminus\{k\}} |\tilde{\mathcal{H}}_{n,k}(\mathbf{z}_n)\sqrt{P_j}|^2 + \sigma} \sqrt{P_k}^H \tilde{\mathcal{H}}_{n,k}^H(q_n^{(\tau+1)}, z_n^{(\tau)}) \tilde{\mathcal{H}}_{n,k}(\mathbf{z}_n)\sqrt{P_k}\} \\
& - \sigma \frac{|\tilde{\mathcal{H}}_{n,k}(q_n^{(\tau+1)}, z_n^{(\tau)})\sqrt{P_k}|^2(|\tilde{\mathcal{H}}_{n,k}(\mathbf{z}_n)\sqrt{P_k}|^2 + \sum_{j\in\mathcal{K}\setminus\{k\}} |\tilde{\mathcal{H}}_{n,k}(\mathbf{z}_n)\sqrt{P_j}|^2)}{(\sum_{j\in\mathcal{K}\setminus\{k\}} |\tilde{\mathcal{H}}_{n,k}(q_n^{(\tau+1)}, z_n^{(\tau)})\sqrt{P_j}|^2 + \sigma)(\sum_{j\in\mathcal{K}} |\tilde{\mathcal{H}}_{n,k}(q_n^{(\tau+1)}, z_n^{(\tau)})\sqrt{P_j}|^2 + \sigma)} \\
\triangleq \quad & \tilde{x}_{1n,k}^{(\tau)} + \frac{2\Re\{\sqrt{P_k}^H \tilde{\mathcal{H}}_{n,k}^H(q_n^{(\tau+1)}, z_n^{(\tau)}) \tilde{\mathcal{H}}_{n,k}(q_n^{(\tau+1)}, z_n^{(\tau)})\sqrt{P_k}\}}{\tilde{a}_{1n,k}^{(\tau+1)}} \\
& - \tilde{\zeta}_{1n,k}^{(\tau)} \sum_{j\in\mathcal{K}} |\tilde{\mathcal{H}}_{n,k}(\mathbf{z}_n)\sqrt{P_k}|^2
\end{aligned} \tag{32}$$

with

$$\begin{aligned}
\tilde{x}_{1n,k}^{(\tau)} &\triangleq r_{n,k}(z_n^{(\tau)}) - \sigma\tilde{a}_{n,k}^{(\tau)} - |\tilde{\mathcal{H}}_{n,k}(q_n^{(\tau+1)}, z_n^{(\tau)})|^2 P_k / \tilde{a}_{n,k}^{(\tau)}, \\
0 < \tilde{\zeta}_{1n,k}^{(\tau)} &\triangleq |\tilde{\mathcal{H}}_{n,k}(q_n^{(\tau+1)}, z_n^{(\tau)})|^2 P_k / (\tilde{a}_{n,k}^{(\tau)} |\tilde{\mathcal{H}}_{k,n}(q_n^{(\tau+1)}, z_n^{(\tau)})|^2 P_k + \tilde{a}_{n,k}^{(\tau)}), \\
\tilde{a}_{1n,k}^{(\tau)} &\triangleq \sum_{j\in\mathcal{K}\setminus\{k\}} |\tilde{\mathcal{H}}_{n,k}(q_n^{(\tau+1)}, z_n^{(\tau)})|P_j^2 + \sigma.
\end{aligned} \tag{33}$$

$\tilde{\mathcal{H}}_{n,k}(\mathbf{z}_n)$ defined in (12) can be represented by the following:

$$\begin{aligned}
\tilde{\mathcal{H}}_{n,k}(\mathbf{z}_n) \quad &\triangleq \quad \tilde{h}_{\mathrm{n,R\text{-}k}} \mathrm{diag}(\mathbf{z}_n) G_{\mathrm{n,U\text{-}R}}(q_n^{(\tau+1)}) \\
&= \quad \sum_{m\in\mathcal{M}} \tilde{h}_{\mathrm{n,R\text{-}k}} \Delta_{n,m} G_{\mathrm{n,U\text{-}R}}(q_n^{(\tau+1)}) \mathbf{z}_{n,m},
\end{aligned} \tag{34}$$

where $\Delta_{n,m}$ is a matrix of size $(M \times M)$ with zero entries everywhere except for its (m,m)-entry, which is one. Therefore, we have:

$$\frac{\Re\{(P_k)^H \tilde{\mathcal{H}}_{n,k}^H(z_n^{(\tau)})\tilde{\mathcal{H}}_{n,k}(q_n^{(\tau+1)},\mathbf{z}_n)P_k\}}{\tilde{a}_{1n,k}^{(\tau)}} = \tilde{y}_{1n,k}^{(\tau)}\mathbf{z}_n, \tag{35}$$

where $\tilde{y}_{1n,k}^{(\tau)} \in \mathbb{C}^{1\times M}$ with the entries

$$\tilde{y}_{1n,k}^{(\tau)}(m) = (P_k)^H \tilde{\mathcal{H}}_{n,k}^H(q_n^{(\tau+1)}, z_n^{(\tau)})\tilde{h}_{\text{n,R-k}}\Delta_{n,m}G_{\text{n,U-R}}(q_n^{(\tau+1)})P_k/\tilde{a}_{1n,k}^{(\tau)}, m \in \mathcal{M}, \tag{36}$$

while

$$\left|\tilde{\mathcal{H}}_{n,k}(\mathbf{z}_n)P_j\right|^2 = \left|\sum_{m=1}^{M}\tilde{b}_{1n,k,j}^{(\tau+1)}(m)\mathbf{z}_{n,m}\right|^2 \tag{37}$$

$$= \sum_{j=1}^{K}\mathbf{z}_n^H\tilde{\Psi}_{1n,k,j}^{(\tau+1)}\mathbf{z}_n \tag{38}$$

where

$$\tilde{b}_{1n,k,j}^{(\tau+1)}(m) = \tilde{h}_{\text{n,R-k}}\Delta_{n,m}G_{\text{n,U-R}}(q_n^{(\tau+1)})P_j, m \in \mathcal{M}, \tag{39}$$

and

$$\tilde{\Psi}_{1n,k,j}^{(\tau+1)}(m,m') \triangleq \left(\tilde{b}_{1n,k,j}^{(\tau+1)}(m)\right)^* \tilde{b}_{1n,k,j}^{(\tau+1)}(m), (m,m') \in \mathcal{M}\times\mathcal{M}. \tag{40}$$

Based on (35) and (38), we can derive the exact concave quadratic form of $\tilde{r}_{k,n}^{(\tau)}(\mathbf{z})$ as defined in (32):

$$\tilde{r}_{1n,k}^{(\tau)}(\mathbf{z}_n) = \tilde{x}_{1n,k}^{(\tau)} + 2\Re\{\tilde{y}_{1n,k}^{(\tau+1)}\mathbf{z}_n\} - \tilde{\zeta}_{1n,k}^{(\tau)}\sum_{j\in\mathcal{K}}\mathbf{z}_n^H\tilde{\Psi}_{1n,k,j}^{(\tau+1)}\mathbf{z}_n. \tag{41}$$

This allows us to find $z_n^{(\tau+1)}$, which satisfies (28) or (29) by solving the following convex problem:

$$\max_{\mathbf{z}_n} f_p[\tilde{r}_{n,1}^{(\tau)}(\mathbf{z}_n), \ldots, \tilde{r}_{n,K}^{(\tau)}(\mathbf{z}_n)] - c||\mathbf{z}_n - e^{\jmath\theta_n^{(\tau)}}||^2. \tag{42}$$

3.3. Quantized Alternating Optimization

By seeking $\theta^{(\tau+1)}$ so that

$$f_{p,c}[q_n^{(\tau+1)}, z_n^{(\tau+1)}, \theta_n^{(\tau+1)}] > f_{p,c}[q_n^{(\tau+1)}, z_n^{(\tau+1)}, \theta_n^{(\tau)}] \tag{43}$$

$$\Leftrightarrow \quad ||z_n^{(\tau+1)} - e^{\jmath\theta_n^{(\tau+1)}}|| > ||z_n^{(\tau+1)} - e^{\jmath\theta_n^{(\tau)}}||, \tag{44}$$

we can solve the following problem

$$\min_{\boldsymbol{\theta}_n} ||z_n^{(\tau+1)}e^{\jmath\boldsymbol{\theta}_n}||^2 \quad \text{s.t.} \quad (14), \tag{45}$$

which has a closed-form solution given by $(\lfloor\angle z_{n,m}^{(\tau+1)}\rceil_b = \nu_b\frac{2\pi}{2^b}$ with $\nu_b \triangleq \arg\min_{\{\nu,\nu+1\}}\left|\nu\frac{2\pi}{2^b} - \angle z_{n,m}^{(\tau+1)}\right|$ for $\angle z_{n,m}^{(\tau+1)} \in [\nu\frac{2\pi}{2^b}, (\nu+1)\frac{2\pi}{2^b}].)$

$$\theta_{n,m}^{(\tau+1)} = \left\lfloor\angle z_{n,m}^{(\tau+1)}\right\rceil_b, m \in \mathcal{M}. \tag{46}$$

4. Passive RIS Reduced-Complexity PRE Optimization for the MR Problem

In this section, the process of generating $z_n^{(\tau+1)}$ is simplified by employing a closed-form expression with scalable complexity. To achieve this, we utilize the following equivalent formulation of (10).

$$\max_{\boldsymbol{\theta}_n} \min_{k\in\mathcal{K}} r_{n,k}(e^{\jmath\boldsymbol{\theta}_n}) \quad \text{s.t.} \quad (14). \tag{47}$$

We denote $(\theta_n^{(\tau)})$ as a point of (47), found from $(\tau-1)$-st round.

Alternating Optimization of the PREs

To seek $\theta^{(\tau+1)}$ so that

$$\min_{k\in\mathcal{K}} r_k(e^{\jmath\theta_n^{(\tau+1)}}) > \min_{k\in\mathcal{K}} r_k(e^{\jmath\theta_n^{(\tau)}}) \tag{48}$$

under the condition that $e^{\jmath\theta_n^{(\tau+1)}} \neq e^{\jmath\theta_n^{(\tau)}}$, we address the subsequent discrete problem:

$$\max_{\boldsymbol{\theta}_n} \min_{k\in\mathcal{K}} r_k(w^{(\tau+1)}, e^{\jmath\boldsymbol{\theta}_n}) \quad \text{s.t.} \quad (14). \tag{49}$$

Let $\tilde{r}_{2n,k}^{(\tau)}(e^{\jmath\boldsymbol{\theta}_n})$ be derived from $\tilde{r}_{1n,k}^{(\tau)}(e^{\jmath\boldsymbol{\theta}_n})$, defined from (41), with $z_n^{(\tau)}$ replaced by $e^{\jmath\theta_n^{(\tau)}}$. Then,

$$\begin{aligned}
r_{2n,k}(e^{\jmath\boldsymbol{\theta}_n}) &\geq \tilde{r}_{2n,k}^{(\tau)}(e^{\jmath\boldsymbol{\theta}_n}) \\
&= \tilde{x}_{1n,k}^{(\tau)} + 2\Re\{\sum_{m\in\mathcal{M}} \tilde{y}_{1n,k}^{(\tau+1)}(m) e^{\jmath\boldsymbol{\theta}_{n,m}}\} - \sum_{j\in\mathcal{K}} (e^{\jmath\boldsymbol{\theta}_n})^H \tilde{\Psi}_{2n,k}^{(\tau+1)} e^{\jmath\boldsymbol{\theta}_n} \\
&\geq \tilde{x}_{1n,k}^{(\tau)} + 2\Re\{\sum_{m\in\mathcal{M}} (\tilde{y}_{1n,k}^{(\tau+1)}(m) - \sum_{m'\in\mathcal{M}} e^{-\jmath\theta_{n,m'}^{(\tau)}} \tilde{\Psi}_{2n,k}^{(\tau+1)}(m',m) + \lambda_{\max}(\tilde{\Psi}_{2n,k}^{(\tau+1)}) \\
&\quad e^{-\jmath\theta_{n,m}^{(\tau)}}) e^{\jmath\boldsymbol{\theta}_{n,m}}\} - (e^{\jmath\theta_n^{(\tau)}})^H \tilde{\Psi}_{2n,k}^{(\tau+1)} e^{\jmath\theta_n^{(\tau)}} - 2M\lambda_{\max}(\tilde{\Psi}_{2n,k}^{(\tau+1)}) \qquad (50) \\
&= \hat{\tilde{x}}_{2n,k}^{(\tau+1)} + 2\sum_{m\in\mathcal{M}} \Re\{\hat{\tilde{y}}_{2n,k}^{(\tau+1)}(m) e^{\jmath\boldsymbol{\theta}_{n,m}}\}, \qquad (51) \\
&\triangleq \hat{r}_{2n,k}^{(\tau)}(e^{\jmath\boldsymbol{\theta}_n}), \qquad (52)
\end{aligned}$$

for

$$\tilde{\Psi}_{2n,k}^{(\tau+1)} \triangleq \tilde{\zeta}_{1n,k}^{(\tau)} \sum_{j\in\mathcal{K}} \tilde{\Psi}_{1n,k,j}^{(\tau+1)},$$

where we have:

$$\hat{\tilde{x}}_{2n,k}^{(\tau+1)} \triangleq \tilde{x}_{1n,k}^{(\tau+1)} - (e^{\jmath\theta_n^{(\tau)}})^H \tilde{\Psi}_{2n,k}^{(\tau+1)} e^{\jmath\theta_n^{(\tau)}} - 2M\lambda_{\max}(\tilde{\Psi}_{2n,k}^{(\tau+1)}),$$

and

$$\hat{\tilde{y}}_{2n,k}^{(\tau+1)}(m) \triangleq \tilde{y}_{2n,k}^{(\tau+1)}(m) - \sum_{m'\in\mathcal{M}} e^{-\jmath\theta_{n,m'}^{(\tau)}} \tilde{\Psi}_{2n,k}^{(\tau+1)}(m',m) + \lambda_{\max}(\tilde{\Psi}_{2n,k}^{(\tau+1)}) e^{-\jmath\theta_{n,m}^{(\tau)}}.$$

Furthermore,

$$\min_{k=1,\ldots,K} \tilde{\tilde{r}}_{2n,k}^{(\tau)}(e^{\jmath\boldsymbol{\theta}_n}) \geq \hat{\tilde{r}}^{(\tau)}(e^{\jmath\boldsymbol{\theta}_n}) \triangleq \min_{k\in\mathcal{K}} \hat{\tilde{x}}_{2n,k}^{(\tau+1)} + 2\sum_{m=1}^{M} \min_{k\in\mathcal{K}} \Re\{\hat{\tilde{y}}_{2n,k}^{(\tau+1)}(m) e^{\jmath\boldsymbol{\theta}_{n,m}}\}. \tag{53}$$

Now, by using $\hat{\bar{r}}^{(\tau)}(\boldsymbol{\theta}_n)$ in (53), we can address the following problem to generate $\theta_n^{(\tau+1),0} \triangleq (\theta_{n,1}^{(\tau+1),0}, \ldots, \theta_{n,M}^{(\tau+1),0})^T$:

$$\max_{\boldsymbol{\theta}_n} \hat{\bar{r}}^{(\tau)}(\boldsymbol{\theta}_n), \tag{54}$$

which is decomposed into M subproblems to find the optimal solution for each element:

$$\max_{\boldsymbol{\theta}_{n,m} \in \mathcal{B}} \min_{k \in \mathcal{K}} \Re\{\hat{\tilde{y}}_k^{(\tau+1)}(m) e^{\jmath \boldsymbol{\theta}_{n,m}}\}. \tag{55}$$

For each PRE, the optimal solution $\theta_{n,m}^{(\tau+1),0}$ can be determined by evaluating $f_{n,m}(\boldsymbol{\theta}_{n,m}) \triangleq \min_{k \in \mathcal{K}} \Re\{\hat{\tilde{y}}_{n,k}^{(\tau+1)}(m) e^{\jmath \boldsymbol{\theta}_{n,m}}\}$ where $\boldsymbol{\theta}_{n,m} \in 2\pi$ at 2^b points. For example, for the first $\boldsymbol{\theta}_{n,1} \in \Delta$ at 2^b points, we can find the minimum value of $\Re\{\hat{\tilde{y}}_{n,k}^{(\tau+1)}(m) e^{\jmath \boldsymbol{\theta}_{n,1}}\}$ for K users. For the second $\boldsymbol{\theta}_{n,2} \in \Delta$ at 2^b points, we can also find the minimum value of $\Re\{\hat{\tilde{y}}_{n,k}^{(\tau+1)}(m) e^{\jmath \boldsymbol{\theta}_{n,2}}\}$ for K users, and so on; in this way, we can obtain m values. Hence, we selected $\boldsymbol{\theta}_{n,m} \in \Delta$, which yields the largest $f_{n,m}(\boldsymbol{\theta}_{n,m})$.

We also solve the following problem to obtain $\theta_n^{(\tau+1),k} \triangleq (\theta_{n,1}^{(\tau+1),k}, \ldots, \theta_{n,M}^{(\tau+1),k})^T$, $k = 0, 1, \ldots, K$, ensuring that $r_{n,k}(e^{\jmath \theta_n^{(\tau+1),k}}) > r_{n,k}(e^{\jmath \theta_n^{(\tau)}})$

$$\max_{\boldsymbol{\theta}_n} \hat{r}_{n,k}^{(\tau)}(e^{\jmath \boldsymbol{\theta}_n}), \tag{56}$$

where the function $\hat{r}_{n,k}^{(\tau)}(e^{\jmath \boldsymbol{\theta}_n})$ in (52) is an affine function of $e^{\jmath \boldsymbol{\theta}_n}$. By noting that $\Re\{a e^{j\theta_n}\} = |a| \cos(\angle a + \theta_n)$, and thus is maximized at $\theta_n = -\angle a$, we obtain the closed-form solution given by

$$\theta_{n,m}^{(\kappa+1),k} = 2\pi - \left\lfloor \angle \hat{\tilde{y}}_{n,k}^{(\tau+1)}(m) \right\rceil_b, m \in \mathcal{M}. \tag{57}$$

Consequently, we obtain $\theta_n^{(\tau+1)}$ from $\theta_n^{(\tau+1),k'}$ for $k' = 0, 1, \ldots, K$ and $\theta_n^{(\tau)}$, which results in the highest $\min_{k \in \mathcal{K}} r_{n,k}(e^{\jmath \boldsymbol{\theta}_n})$, i.e.,

$$\theta_n^{(\tau+1)} \triangleq \underset{\boldsymbol{\theta}_n \in \{\theta_n^{(\tau+1),k'}, k'=0,1,\ldots K\} \cup \{\theta_n^{(\tau)}\}}{\arg\max} \min_{k \in \mathcal{K}} r_k(e^{\jmath \boldsymbol{\theta}_n}), \tag{58}$$

to validate (48). This is valid as long as $\theta_n^{(\tau+1)} \neq \theta_n^{(\tau)}$.

5. Active RIS Convex-Solver-Based Algorithms

In this section, alternate optimization is implemented for each set of variables ($\bar{\mathbf{q}}_n$,$\bar{\mathbf{z}}_n$, $\boldsymbol{p}_n$, $\bar{\boldsymbol{\theta}}_n$) while keeping the others fixed to generate the next iterative point. Starting with the feasible point obtained by initializing (20) as $(\bar{q}_n^{(0)}, z_n^{(0)}, \theta_n^{(0)})$, we let $(q_n^{(\tau)}, z_n^{(\tau)}, \theta_n^{(\tau)})$ represent a feasible point for (20), found in the $(\tau-1)$-st iteration.

5.1. Alternating Optimization of UAV Trajectory

To seek $\bar{\mathbf{q}}_n^{(\tau+1)}$ such that

$$\bar{f}_{a,\rho}[\bar{q}_n^{(\tau+1)}, \bar{z}_n^{(\tau+1)}, p_n^{(\tau)}, \bar{\theta}_n^{(\tau)}] > \bar{f}_{a,\rho}[\bar{q}_n^{(\tau)}, \bar{z}_n^{(\tau)}, p_n^{(\tau)}, \bar{\theta}_n^{(\tau)}], \tag{59}$$

the trajectory optimization subproblem can be reformulated as follows:

$$\max_{\bar{\mathbf{q}}_n} \min_k \quad \frac{1}{N} \sum_{n=1}^{N} \ln\left(1 + \frac{|\tilde{\bar{\mathcal{H}}}_{n,k}(\bar{\mathbf{q}}_n)|^2 P_k}{\sum_{j \in \mathcal{K} \setminus \{k\}} |\tilde{\bar{\mathcal{H}}}_{n,k}(\bar{\mathbf{q}}_n)|^2 P_j + D_n}\right) \tag{60a}$$

$$\text{s.t.} \quad (1)\text{–}(2), \tag{60b}$$

where $D_n = \sigma_v \sum_{m\in\mathcal{M}} |\tilde{h}_{\text{n,R-k}}(m)|^2 |\bar{z}_{n,m}|^2 + \sigma$. The slack variable u is introduced, and problem (60) can be reformulated as follows:

$$\max_{\bar{\mathbf{q}}_n, s} \quad u \tag{61a}$$

$$\text{s.t.} \quad (1)\text{–}(2), \tag{61b}$$

$$\frac{1}{N}\sum_{n=1}^{N} \ln\left(1 + \frac{|\tilde{\bar{\mathcal{H}}}_{n,k}(\bar{\mathbf{q}}_n)|^2 P_k}{\sum_{j\in\mathcal{K}\setminus\{k\}} |\tilde{\bar{\mathcal{H}}}_{n,k}(\bar{\mathbf{q}}_n)|^2 P_j + D_n}\right) \geq u, \forall k \in \mathcal{K}. \tag{61c}$$

Subsequently, the problem (61) can be transformed as follows:

$$\max_{\bar{\mathbf{q}}_n, s} \quad u \tag{62a}$$

$$\text{s.t.} \quad (1)\text{–}(2), \tag{62b}$$

$$\frac{1}{N}\sum_{n=1}^{N} \ln\left(1 + \frac{A_{n,k}^{aR(\tau)}}{B_{n,k}^{aR(\tau)} + d_{n,U-R}^{\kappa}}\right) \geq u, \forall k \in \mathcal{K}. \tag{62c}$$

where $A_{n,k}^{aR(\tau)} = |\tilde{h}_{\text{n,R-k}}\text{diag}(\mathbf{z}_n^{\tau})\sqrt{\beta_0}G_{\text{U-R,n}}|^2 P_k/\sigma$, $B_{n,k}^{aR(\tau)} = \sum_{j\in\mathcal{K}\setminus\{k\}} |\tilde{h}_{\text{n,R-j}}\text{diag}(\mathbf{z}_n^{\tau})\sqrt{\beta_0} G_{\text{U-R,n}}|^2 P_j/\sigma + \sigma_v \sum_{m\in\mathcal{M}} |\tilde{h}_{\text{n,R-k}}(m)|^2 |\bar{z}_{n,m}|^2/\sigma$ and $d_{n,U-R}^{\kappa} = \|\bar{\mathbf{q}}_n - \boldsymbol{w}_r\|^{\kappa}$.

However, the problem (62) cannot be solved directly due to the nonconvex constraint (62c). Similarly, the lower bound of the left-hand side of the constraint (62c) can be derived at the feasible point $\bar{\mathbf{q}}_n^r$

$$\begin{aligned}\frac{1}{N}\sum_{n=1}^{N} \ln\left(1 + \frac{A_{n,k}^{aR(\tau)}}{B_{n,k}^{aR(\tau)} + d_{n,U-R}^{\tau}}\right) \geq & \frac{1}{N}\sum_{n=1}^{N} \ln\left(1 + \frac{A_{n,k}^{aR(\tau)}}{B_{n,k}^{aR(\tau)} + d_{n,U-R}^{r,\tau}}\right) \\ & + \frac{A_{n,k}^{aR(\tau)}}{A_{n,k}^{aR(\tau)} + B_{n,k}^{aR(\tau)} + d_{n,U-R}^{r,\tau}}\left(1 - \frac{d_{n,U-R}^{\tau}}{d_{n,U-R}^{r,\tau}}\right) \\ \triangleq & \tilde{R}_k^{aR,lb},\end{aligned} \tag{63}$$

Thus, the trajectory optimization problem can be expressed as follows:

$$\max_{\bar{\mathbf{q}}_n, s} \quad s \tag{64a}$$

$$\text{s.t.} \quad (1)\text{–}(2), \tag{64b}$$

$$\tilde{R}_k^{aR,lb} \geq u, \forall k \in \mathcal{K}. \tag{64c}$$

5.2. Alternating Optimization of the Power-Amplified PREs

To seek $z_n^{(\tau+1)}$ such that

$$\bar{f}_{a,\rho}[\bar{q}_n^{(\tau+1)}, \bar{z}_n^{(\tau+1)}, p_n^{(\tau)}, \bar{\theta}_n^{(\tau)}] > \bar{f}_{a,\rho}[\bar{q}_n^{(\tau+1)}, \bar{z}_n^{(\tau)}, p_n^{(\tau)}, \bar{\theta}_n^{(\tau)}] \Leftrightarrow \tag{65}$$

$$\bar{f}_a[\bar{r}_n(z_n^{(\tau+1)})] - \rho \sum_{m\in\mathcal{M}} |\bar{z}_{n,m}^{(\tau)} - p_{n,m}^{(\tau)} e^{j\bar{\theta}_{n,m}^{(\tau)}}|^2 > \bar{f}_a[\bar{r}_n(z_n^{(\tau)})] - \rho \sum_{m\in\mathcal{M}} |\bar{z}_{n,m}^{(\tau)} - p_{n,m}^{(\tau)} e^{j\bar{\theta}_{n,m}^{(\tau)}}|^2, \tag{66}$$

We now consider an unconstrained optimization problem:

$$\max_{\bar{\mathbf{z}}_n} \ \bar{f}_{a,\rho} \triangleq \left[\min_{k\in\mathcal{K}} \bar{r}_{n,k}(\bar{\mathbf{z}}) - \rho \sum_{m\in\mathcal{M}} |\bar{\mathbf{z}}_{n,m} - p_{n,m}^{(\tau)} e^{j\bar{\theta}_{n,m}^{(\tau)}}|^2\right] \quad \text{s.t.} \quad (18), \tag{67}$$

where, as per (16), we obtain:

$$\bar{r}_{n,k}(\bar{\mathbf{z}}_n) = \ln\left(1 + \frac{|\tilde{\bar{\mathcal{H}}}_{n,k}(\bar{\mathbf{z}}_n)\sqrt{P_k}|^2}{\sum_{j\in\mathcal{K}\setminus\{k\}}|\tilde{\bar{\mathcal{H}}}_{n,k}(\bar{\mathbf{z}}_n)\sqrt{P_j}|^2 + \sigma_\nu\sum_{m\in\mathcal{M}}|\tilde{h}_{\text{n,R-k}}(m)|^2|\bar{\mathbf{z}}_{n,m}|^2 + \sigma}\right), k \in \mathcal{K}. \tag{68}$$

Using the inequality (A2) for $(\boldsymbol{a}, \boldsymbol{b}) = (\tilde{\bar{\mathcal{H}}}_{n,k}(\mathbf{z}_n)\sqrt{P_k}, \sum_{j\in\mathcal{K}\setminus\{k\}}|\tilde{\bar{\mathcal{H}}}_{n,k}(\mathbf{z}_n)\sqrt{P_j}|^2)$ and $(\bar{a}, \bar{b}) = (\tilde{\bar{\mathcal{H}}}_{n,k}(q_n^{(\tau+1)}, z_n^{(\tau)})\sqrt{P_k}, \sum_{j\in\mathcal{K}\setminus\{k\}}|\tilde{\bar{\mathcal{H}}}_{n,k}(q_n^{(\tau+1)}, z_n^{(\tau)})\sqrt{P_j}|^2)$, we can obtain a concave quadratic function with approximating $\bar{r}_{k,n}(\bar{\mathbf{z}}_n)$.

$$\begin{aligned}
\tilde{\bar{r}}_{n,k}^{(\tau)}(\bar{\mathbf{z}}_n) \triangleq\ & \ln(1 + \frac{|\tilde{\bar{\mathcal{H}}}_{n,k}(\bar{q}_n^{(\tau+1)}, \bar{z}_n^{(\tau)})\sqrt{P_k}|^2}{\sum_{j\in\mathcal{K}\setminus\{k\}}|\tilde{\bar{\mathcal{H}}}_{n,k}(\bar{q}_n^{(\tau+1)}, \bar{z}_n^{(\tau)})\sqrt{P_j}|^2 + \sigma}) \\
& - \frac{|\tilde{\bar{\mathcal{H}}}_{n,k}(\bar{q}_n^{(\tau+1)}, \bar{z}_n^{(\tau)})\sqrt{P_k}|^2}{\sum_{j\in\mathcal{K}\setminus\{k\}}|\tilde{\bar{\mathcal{H}}}_{n,k}(\bar{q}_n^{(\tau+1)}, \bar{z}_n^{(\tau)})\sqrt{P_j}|^2 + \sigma} \\
& - \sigma\frac{|\tilde{\bar{\mathcal{H}}}_{n,k}(\bar{q}_n^{(\tau+1)}, \bar{z}_n^{(\tau)})\sqrt{P_k}|^2}{(\sum_{j\in\mathcal{K}\setminus\{k\}}|\tilde{\bar{\mathcal{H}}}_{n,k}(\bar{q}_n^{(\tau+1)}, \bar{z}_n^{(\tau)})\sqrt{P_j}|^2 + \sigma)(\sum_{j\in\mathcal{K}}|\tilde{\bar{\mathcal{H}}}_{n,k}(q_n^{(\tau+1)}, z_n^{(\tau)})\sqrt{P_j}|^2 + \sigma)} \\
& + \frac{2}{\sum_{j\in\mathcal{K}\setminus\{k\}}|\tilde{\bar{\mathcal{H}}}_{n,k}(\bar{\mathbf{z}}_n)\sqrt{P_j}|^2 + \sigma}\sqrt{P_k}^H\tilde{\mathcal{H}}_{n,k}^H(\bar{q}_n^{(\tau+1)}, \bar{z}_n^{(\tau)})\tilde{\bar{\mathcal{H}}}_{n,k}(\bar{\mathbf{z}}_n)\sqrt{P_k}\} \\
& - \sigma\frac{|\tilde{\bar{\mathcal{H}}}_{n,k}(\bar{q}_n^{(\tau+1)}, \bar{z}_n^{(\tau)})\sqrt{P_k}|^2(|\tilde{\bar{\mathcal{H}}}_{n,k}(\bar{\mathbf{z}}_n)\sqrt{P_k}|^2 + \sum_{j\in\mathcal{K}\setminus\{k\}}|\tilde{\bar{\mathcal{H}}}_{n,k}(\bar{\mathbf{z}}_n)\sqrt{P_j}|^2)}{(\sum_{j\in\mathcal{K}\setminus\{k\}}|\tilde{\bar{\mathcal{H}}}_{n,k}(\bar{q}_n^{(\tau+1)}, \bar{z}_n^{(\tau)})\sqrt{P_j}|^2 + \sigma)(\sum_{j\in\mathcal{K}}|\tilde{\bar{\mathcal{H}}}_{n,k}(\bar{q}_n^{(\tau+1)}, \bar{z}_n^{(\tau)})\sqrt{P_j}|^2 + \sigma)} \\
\triangleq\ & \tilde{\bar{x}}_{n,k}^{(\tau)} + \frac{2\Re\{P_k^H\tilde{\bar{\mathcal{H}}}_{n,k}^H(\bar{q}_n^{(\tau+1)}, \bar{z}_n^{(\tau)})\tilde{\bar{\mathcal{H}}}_{n,k}(\bar{\mathbf{z}}_n)P_k\}}{\tilde{\bar{a}}_{n,k}^{(\tau+1)}} - \tilde{\bar{\zeta}}_{n,k}^{(\tau)}\sum_{j\in\mathcal{K}}|\tilde{\bar{\mathcal{H}}}_{n,k}(\bar{\mathbf{z}}_n)|^2P_k,
\end{aligned} \tag{69}$$

with

$$\begin{aligned}
\tilde{\bar{x}}_{n,k}^{(\tau)} &\triangleq r_{n,k}(\bar{z}_n^{(\tau)}) - \sigma\tilde{\bar{a}}_{n,k}^{(\tau+1)} - |\tilde{\bar{\mathcal{H}}}_{n,k}(\bar{z}_n^{(\tau)})|^2P_k/\tilde{\bar{a}}_{n,k}^{(\tau+1)}, \\
0 < \tilde{\bar{\zeta}}_{n,k}^{(\tau)} &\triangleq |\tilde{\bar{\mathcal{H}}}_{n,k}(\bar{\mathbf{z}}_n)|^2P_k/(\tilde{\bar{a}}_{n,k}^{(\tau+1)}|\tilde{\mathcal{H}}_{k,n}(\bar{z}_n^{(\tau)})|^2P_k + \tilde{\bar{a}}_{n,k}^{(\tau+1)})), \\
\tilde{\bar{a}}_{n,k}^{(\tau+1)} &\triangleq \sum_{j\in\mathcal{K}\setminus\{k\}}|\tilde{\bar{\mathcal{H}}}_{n,k}(\bar{z}_n^{(\tau)})|P_j^2 + \sigma.
\end{aligned} \tag{70}$$

We thus generate $\bar{z}_n^{(\tau+1)}$, verifying (69) by solving the following convex quadratic problem:

$$\max_{\bar{\mathbf{z}}_n}\left[\min_{k\in\mathcal{K}}\tilde{\bar{r}}_{n,k}^{(\tau)}(\bar{\mathbf{z}}_n) - \rho\sum_{m\in\mathcal{M}}|\bar{z}_{n,m} - p_{n,m}^{(\tau)}e^{\jmath\bar{\theta}_{n,m}^{(\tau)}}|^2\right] \quad \text{s.t.} \quad (18). \tag{71}$$

5.3. Alternating Optimization of Amplifier and PREs

We generate $p_n^{(\tau+1)}$ and $\bar{\theta}_n^{(\tau+1)}$ by

$$p_{n,m}^{(\tau+1)} = \arg\min_{\boldsymbol{p}_{n,m}}|\bar{z}_{n,m}^{(\tau+1)} - \boldsymbol{p}_{n,m}e^{\jmath\bar{\theta}_{n,m}^{(\tau)}}|^2 = |\bar{z}_{n,m}^{(\tau+1)}|\cos(\angle\bar{z}_n^{(\tau+1)} - \bar{\theta}_{n,m}^{(\tau)}), m \in \mathcal{M}, \tag{72}$$

and

$$\bar{\theta}_{n,m}^{(\tau+1)} = \arg\min_{\bar{\boldsymbol{\theta}}_{n,m}\in\mathcal{B}}|\bar{z}_{n,m}^{(\tau+1)} - p_{n,m}^{(\tau+1)}e^{\jmath\bar{\boldsymbol{\theta}}_{n,m}}|^2 = \lfloor\angle\bar{z}_{n,m}^{(\tau+1)}\rceil_b, \tag{73}$$

which yields

$$\begin{aligned}
\bar{f}_{a,\rho}(\bar{q}_n^{(\tau+1)}, \bar{z}_n^{(\tau+1)}, p_n^{(\tau+1)}, \bar{\theta}_n^{(\tau+1)}) &> \bar{f}_{a,\rho}(\bar{q}_n^{(\tau+1)}, \bar{z}_n^{(\tau+1)}, p_n^{(\tau+1)}, \bar{\theta}_n^{(\tau)}) \\
&> \bar{f}_{a,\rho}(\bar{q}_n^{(\tau+1)}, z_n^{(\tau+1)}, p_n^{(\tau)}, \bar{\theta}_n^{(\tau)}).
\end{aligned} \tag{74}$$

6. Numerical Examples

Furthermore, the spatial correlation matrix of RIS i is given by the following:

$$[R_{\text{R-k}}]_{m,m'} = e^{j\pi(m-m')\sin\tilde{\psi}_k \sin\tilde{\theta}_k}, \tag{75}$$

where $\tilde{\psi}_k$ and $\tilde{\theta}_k$ represent the azimuth and elevation angles of user k, respectively. The horizontal initial point and end point of the UAV are $[-100, 20]^T$ and $[100.20]^T$, respectively. The locations of RIS and GUs are set as $[0, 0, 40]^T$, $[-80, 60, 0]^T$, $[-60, 40, 0]^T$, $[-40, 50, 0]^T$, $[40, 50, 0]^T$, $[60, 40, 0]^T$, $[80, 60, 0]^T$, respectively. The maximum speed of the UAV is 25 m/s and the altitude of the UAV is 80 m. $\beta_0 = -30$ dB and $\kappa = 2$, while white noise $\sigma = -90$ dBm. The time slot $\delta_t = 1$ s. Unless specified otherwise, we assume that the transmit power is $P_k = P_{out} = 20$dBm, $k \in \mathcal{K}$, flight time is $T = 50$ s, the aRIS power is $P_A = 0.01P_{out}$, the number of RIS elements is $M = M_x \times M_z = 10 \times 10$, and the PRE resolution is $b = 3$.

For the simulation, we used Matlab R2022a along with the CVX solver. Our proposed algorithms are readily adaptable to other programming languages, including "C++ " and "Python". Below, we use the following legends to specify the proposed implementations:

- CVX-based MR RIS/aRIS denotes the performance achieved by Algorithms 1 and 2, respectively, which relies on Matlab 2022a along with the CVX solver to solve the problem (11)/(22) and addresses the MR problem with RIS/aRIS equipped with 3-bit quantized PREs.
- Partially scalable MR RIS represents the performance of Algorithm 3, which employs an iterative approach involving the convex problem (27) and the closed-form expression (58) to address the MR problem (11) using RIS with 3-bit quantized PREs.

Algorithm 1 CVX-based algorithm for computing (11)

1: **Initialization:** Initialize the UAV trajectory $q_n^{(0)}$ with constraints (1)–(2). Randomly generate $(z_n^{(0)}, \theta_n^{(0)})$ feasible for (11), with the fixed UAV trajectory $q_n^{(0)}$. Set $\tau = 0$.
2: **Repeat:**
3: **UAV trajectory design:** Generate $q_n^{(\tau+1)}$ by solving the problem (27) with fixed $(z_n^{(\tau)}, \theta_n^{(\tau)})$.
4: **Repeat until objective value of problem (11) reaches convergence:** with a fixed UAV trajectory $q_n^{(\tau+1)}$, generate $z_n^{(\tau+1)}$ by solving the convex problem (42), and $\theta_n^{(\tau+1)}$ by (9). Reset $\tau \leftarrow \tau + 1$.
5: **Until:** The objective value of problem (11) reaches convergence.
6: **Output** $(e^{\jmath\theta_n^{(\tau)}}, q_n^{(\tau)})$ and $r_{n,k}(q_n^{(\tau)}, e^{\jmath\theta_n^{(\tau)}})$, $k \in \mathcal{K}$.

Algorithm 2 CVX-based algorithm for computing (22)

1: **Initialization:** Initialize the UAV trajectory $q_n^{(0)}$ with constraints (1)–(2). Randomly generate $(z_n^{(0)}, p_n^{(0)}, \theta_n^{(0)})$, feasible for (22). Set $\tau = 0$.
2: **Repeat:**
3: **UAV trajectory design:** Generate $q_n^{(\tau+1)}$ by solving the problem (64) with fixed $(z_n^{(\tau)}, \theta_n^{(\tau)})$.
4: **Repeat until objective value of problem (20) reaches convergence:** with a fixed UAV trajectory $q_n^{(\tau+1)}$, generate $\bar{z}_n^{(\tau+1)}$ by solving the convex problem (71). Generate $(p_n^{(\tau+1)}, \bar{\theta}_n^{(\tau+1)})$ by (72)–(73). Reset $\tau \leftarrow \tau + 1$.
5: **Until:** The objective value of problem (20) reaches convergence.
6: **Output** $(q_n^{(\tau)}, z_n^{(\tau)}, p_n^{(\tau)}, \bar{\theta}_n^{(\tau)})$ and $r_k(q_n^{(\tau)}, \bar{z}_n^{(\tau)})$, $k \in \mathcal{K}$.

Algorithm 3 Partially scalable MR algorithm

1: **Initialization:** Initialize the UAV trajectory $q_n^{(0)}$ with constraints (1)–(2). Randomly generate a feasible $(\theta^{(0)})$ for (47). Set $\tau = 0$.
2: **Repeat:**
3: **UAV trajectory design:** Generate $q_n^{(\tau+1)}$ by solving the problem (27) with fixed $(z_n^{(\tau)}, \theta_n^{(\tau)})$.
4: **Repeat until objective value of problem (11) reaches convergence:** with a fixed UAV trajectory $q_n^{(\tau+1)}$, generate $z_n^{(\tau+1)}$ by solving the convex problem (58). Reset $\tau \leftarrow \tau + 1$.
5: **Until:** The objective value of problem (11) reaches convergence.
6: **Output** $(q_n^{\tau}, e^{j\theta_n^{(\tau)}})$ and rates $r_{n,k}(q_n^{\tau}, e^{j\theta_n^{(\tau)}})$, $k = 1, \ldots, K$.

Figure 2 illustrates the convergence of the proposed algorithms, demonstrating that the objective functions increase with the number of iterations and gradually converge within 25 iterations. The practicality of the proposed algorithms can be observed.

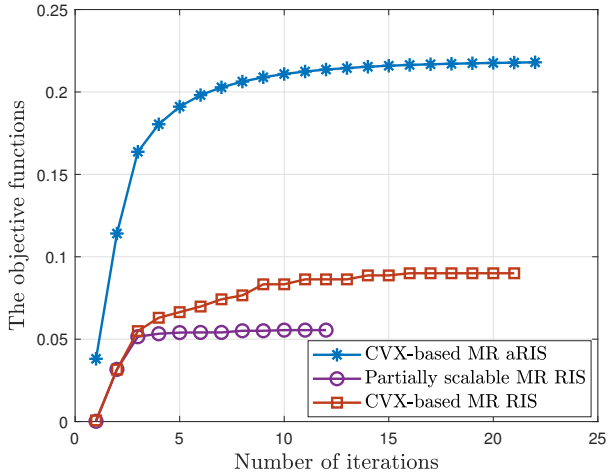

Figure 2. The convergence of the proposed algorithms.

"Table 1 presents the average computational time of the proposed algorithms, measured using a CPU with a 3.7 GHz Intel Core i9 and 32 GB RAM. Algorithm 3 is based on our partially scalable complexity iterations. These can run more than 20 times faster than Algorithm 1, which is based on cubic-complexity iterations, confirming the superiority of scalable complexity iterations".

Table 1. The average computational time to reach 70% of the optimal performance within the proposed algorithms with the same parameter settings.

Algorithm 1	**Algorithm 2**	**Algorithm 3**
4.74 h	4.87 h	0.19 h

Figure 3 plots the min-rate increase in line with the transmit power budget P_{out}. The min-rate increases with the increase in transmit power budget P_{out}. Figure 3 reveals that CVX-based MR aRIS significantly outperforms both CVX-based MR RIS and partially scalable MR RIS. It can be seen that CVX-based MR RIS achieves a better min-rate than partially scalable MR RIS. It can be also seen that MR RIS with random θ_n exhibits the poorest performance.

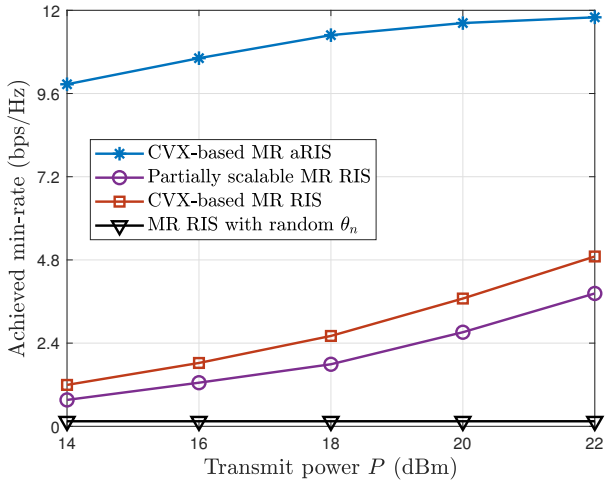

Figure 3. Achieved min-rate versus transmit power, P_{out}.

Figure 4 plots the achievable min-rate upon varying the number of RIS elements M_x, M_z. Figure 4 shows that CVX-based MR aRIS achieves the highest min-rate, while MR RIS with random θ_n attains the lowest min-rate. It can be observed that the min-rate achieved by CVX-based MR RIS is better than that of partially scalable MR RIS. As expected, all the algorithms benefit from an increase in the number of RIS elements, leading to performance improvements.

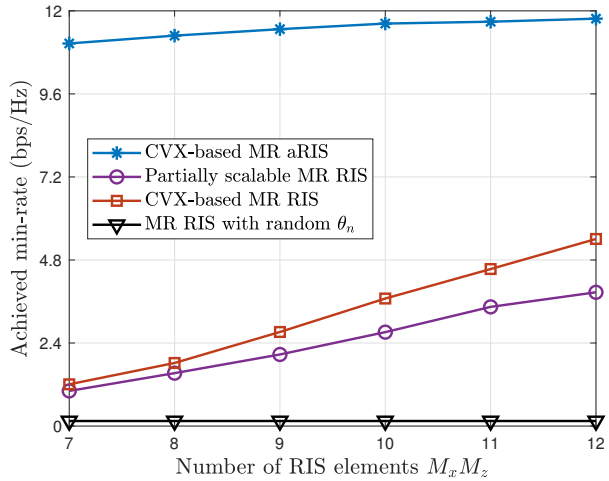

Figure 4. Achieved min-rate versus the number of RIS elements M_x, M_z.

Figure 5 plots the achievable min-rate versus the flight time T. With the increase in flight time, the achieved min-rate increases. It can be observed that the performance of MR aRIS outperforms other algorithms because active RIS can not only tune the phase of the reflected signals, but can also amplify the power of the reflected signals. As expected, MR RIS with random θ_n is the worst performer.

Figure 6 plots the UAV trajectory of different algorithms. It can be seen that the trajectories of the proposed algorithms closely align with the RIS positions, with the UAV hovering in close proximity to the RIS. This behavior minimizes path fading due to the reduced distance between the UAV and the RIS, thereby improving the communication rate.

Figure 7 plots the min-rate attained by the b-bit solution for various values of b. It can be observed that when b increases, there is only a marginal improvement. This observation highlights the ability of the proposed algorithms to achieve equitable minimum rates even at low resolutions.

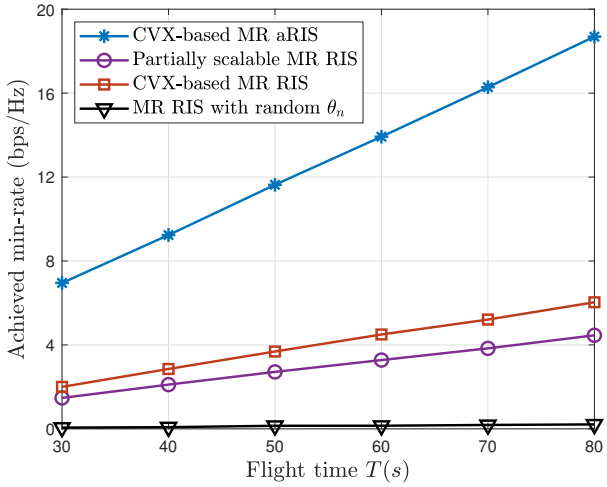

Figure 5. Achieved min-rate versus the flight time T.

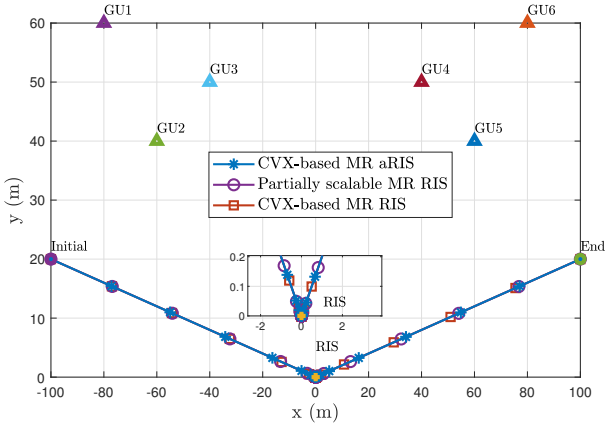

Figure 6. Optimized UAV trajectory of different algorithms.

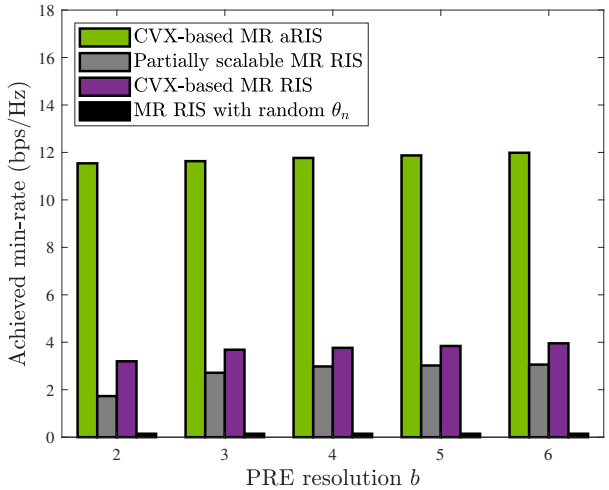

Figure 7. Achieved min-rate versus the reflection coefficient resolution b.

7. Summary and Conclusions

This paper explores the utilization of RIS to boost multiuser communication within UAV networks, aiming to maximize the worst-case user rate. Initially, the study delves into passive RIS, addressing the non-convex optimization problem through a two-stage algorithm. This algorithm decomposes the optimization into trajectory and phase optimization subproblems, leveraging the SCA method to convert them into convex forms. Notably,

the paper contributes a closed-form solution for phase optimization in passive RIS configurations, simplifying the process. Expanding its scope, the investigation further examines aRIS-assisted multiuser communication within UAV systems. Employing a sophisticated optimization approach that combines SCA and alternate optimization, the study identifies local optimal solutions. The simulation experiments that were conducted validate the superior performance of the UAV-aRIS strategy compared to alternative approaches.The results demonstrate the significant potential of RIS in enhancing UAV communication systems, particularly in multiuser scenarios. The contributions of this paper, including the closed-form solution and the optimized algorithm, provide valuable insights for future research in this area.

Author Contributions: Conceptualization, Q.Y. and Y.C.; methodology, Y.C.; software, Q.Y.; validation, Z.H., H.Y. and Y.F.; formal analysis, Y.F.; investigation, H.Y.; writing—original draft preparation, Z.H.; writing—review and editing, Z.H.; supervision, H.Y.; project administration, Y.F. All authors have read and agreed to the published version of the manuscript.

Funding: This work was supported in part by the National Natural Science Foundation of China (NSFC) under Grant 61601282 and in part by the Shanghai Sailing Scholar under Grant 23YF1412700.

Data Availability Statement: Data are contained within the article.

Conflicts of Interest: The authors declare no conflicts of interest.

Appendix A

The following result [40] is used

$$\ln(1+1/\boldsymbol{x}) \geq \ln(1+1/\bar{x}) + \frac{1}{(\bar{x}+1)}\left(1-\frac{\boldsymbol{x}}{\bar{x}}\right), \quad \forall \boldsymbol{x} \in \mathbb{R}_+^2, \bar{x} \in \mathbb{R}_+^2. \tag{A1}$$

The paper utilizes the following matrix inequality [41] for $\boldsymbol{a} \in \mathbb{C}$, $\bar{a} \in \mathbb{C}$, $\boldsymbol{b} \geq 0$, $\bar{b} \geq 0$, and $\sigma > 0$:

$$\begin{aligned} \ln\left(1+\frac{|\boldsymbol{a}|^2}{\boldsymbol{b}+\sigma}\right) \quad \geq \quad & \ln\left(1+\frac{|\bar{a}|^2}{\bar{b}+\sigma}\right) - \frac{|\bar{a}|^2}{\bar{b}+\sigma} - \sigma\frac{|\bar{a}|^2}{(\bar{b}+\sigma)(|\bar{a}|^2+\bar{b}+\sigma)} \\ & + \frac{2}{\bar{b}+\sigma}\Re\{\bar{a}^*\boldsymbol{a}\} - \frac{|\bar{a}|^2}{(\bar{b}+\sigma)(|\bar{a}|^2+\bar{b}+\sigma)}(|\boldsymbol{a}|^2+\boldsymbol{b}). \end{aligned} \tag{A2}$$

References

1. Zhang, H.; Saad, W.; Debbah, M.; Song, L. Guest editorial: Cellular Internet of UAVs for 5G and beyond. *IET Commun.* **2021**, *15*, 1259–1261. [CrossRef]
2. Gupta, L.; Jain, R.; Vaszkun, G. Survey of Important Issues in UAV Communication Networks. *IEEE Commun. Surv. Tut.* **2016**, *18*, 1123–1152. [CrossRef]
3. Liao, N.; He, P.; Du, Y.; Zhang, Y.; Chen, Y.; Liang, T. Joint mission planning and spectrum resources optimization for multi-UAV reconnaissance. *IET Commun.* **2023**, *17*, 324–335. [CrossRef]
4. Xiao, Z.; Zhu, L.; Liu, Y.; Yi, P.; Zhang, R.; Xia, X.G.; Schober, R. A Survey on Millimeter-Wave Beamforming Enabled UAV Communications and Networking. *IEEE Commun. Surv. Tut.* **2022**, *24*, 557–610. [CrossRef]
5. Sheng, Z.; Tuan, H.D.; Duong, T.Q.; Hanzo, L. UAV-Aided Two-Way Multi-User Relaying. *IEEE Trans. Commun.* **2021**, *69*, 246–260. [CrossRef]
6. Yuan, Z.; Jiang, K.; Jia, W.; Liu, R.; Wang, Z.; Mao, X. Interference coordination and throughput maximisation in an unmanned aerial vehicle-assisted cellular: User association and three-dimensional trajectory optimisation. *IET Commun.* **2021**, *15*, 1273–1286. [CrossRef]
7. Zeng, Y.; Zhang, R.; Lim, T.J. Throughput Maximization for UAV-Enabled Mobile Relaying Systems. *IEEE Trans. Commun.* **2016**, *64*, 4983–4996. [CrossRef]
8. Zeng, Y.; Zhang, R. Energy-Efficient UAV Communication with Trajectory Optimization. *IEEE Trans. WireL. Commun.* **2017**, *16*, 3747–3760. [CrossRef]
9. Wang, Y.; Chen, M.; Pan, C.; Wang, K.; Pan, Y. Joint Optimization of UAV Trajectory and Sensor Uploading Powers for UAV-Assisted Data Collection in Wireless Sensor Networks. *IEEE Internet Things J.* **2022**, *9*, 11214–11226. [CrossRef]

10. Zeng, Y.; Xu, X.; Zhang, R. Trajectory Design for Completion Time Minimization in UAV-Enabled Multicasting. *IEEE Trans. Wirel. Commun.* **2018**, *17*, 2233–2246. [CrossRef]
11. Song, Q.; Jin, S.; Zheng, F.C. Completion Time and Energy Consumption Minimization for UAV-Enabled Multicasting. *IEEE Wirel. Commun. Lett.* **2019**, *8*, 821–824. [CrossRef]
12. Li, M.; Jia, G.; Li, X.; Qiu, H. Efficient Trajectory Planning for Optimizing Energy Consumption and Completion Time in UAV-Assisted IoT Networks. *Mathematics* **2023**, *11*, 4399. [CrossRef]
13. Yang, L.; Meng, F.; Zhang, J.; Hasna, M.O.; Renzo, M.D. On the Performance of RIS-Assisted Dual-Hop UAV Communication Systems. *IEEE Trans. Vehic. Techn.* **2020**, *69*, 10385–10390. [CrossRef]
14. Guo, K.; An, K. On the Performance of RIS-Assisted Integrated Satellite-UAV-Terrestrial Networks with Hardware Impairments and Interference. *IEEE Wirel. Commun. Lett.* **2022**, *11*, 131–135. [CrossRef]
15. Mei, H.; Yang, K.; Shen, J.; Liu, Q. Joint Trajectory-Task-Cache Optimization with Phase-Shift Design of RIS-Assisted UAV for MEC. *IEEE Wirel. Commun. Lett.* **2021**, *10*, 1586–1590. [CrossRef]
16. Guo, J.; Yu, L.; Chen, Z.; Yao, Y.; Wang, Z.; Wang, Z.; Zhao, Q. RIS-assisted secure UAV communications with resource allocation and cooperative jamming. *IET Commun.* **2022**, *16*, 1582–1592. [CrossRef]
17. Zhang, H.; Di, B.; Bian, K.; Han, Z.; Poor, H.V.; Song, L. Toward Ubiquitous Sensing and Localization with Reconfigurable Intelligent Surfaces. *Proc. IEEE* **2022**, *110*, 1401–1422. [CrossRef]
18. Huang, C.; Hu, S.; Alexandropoulos, G.C.; Zappone, A.; Yuen, C.; Zhang, R.; Renzo, M.D.; Debbah, M. Holographic MIMO Surfaces for 6G Wireless Networks: Opportunities, Challenges, and Trends. *IEEE Wirel. Commun.* **2020**, *27*, 118–125. [CrossRef]
19. Pan, C.; Ren, H.; Wang, K.; Kolb, J.F.; Elkashlan, M.; Chen, M.; Di Renzo, M.; Hao, Y.; Wang, J.; Swindlehurst, A.L.; et al. Reconfigurable Intelligent Surfaces for 6G Systems: Principles, Applications, and Research Directions. *IEEE Commun. Mag.* **2021**, *59*, 14–20. [CrossRef]
20. Li, S.; Duo, B.; Yuan, X.; Liang, Y.C.; Di Renzo, M. Reconfigurable Intelligent Surface Assisted UAV Communication: Joint Trajectory Design and Passive Beamforming. *IEEE Wirel. Commun. Lett.* **2020**, *9*, 716–720. [CrossRef]
21. Basharat, S.; Khan, M.; Iqbal, M.; Hashmi, U.S.; Zaidi, S.A.R.; Robertson, I. Exploring reconfigurable intelligent surfaces for 6G: State-of-the-art and the road ahead. *IET Commun.* **2022**, *16*, 1458–1474. [CrossRef]
22. Hassouna, S.; Jamshed, M.A.; Rains, J.; Kazim, J.u.R.; Rehman, M.U.; Abualhayja, M.; Mohjazi, L.; Cui, T.J.; Imran, M.A.; Abbasi, Q.H. A survey on reconfigurable intelligent surfaces: Wireless communication perspective. *IET Commun.* **2023**, *17*, 497–537. [CrossRef]
23. Chen, P.; Shi, L.; Fang, Y.; Lau, F.C.M.; Cheng, J. Rate-Diverse Multiple Access Over Gaussian Channels. *IEEE Trans. Wirel. Commun.* **2023**, *22*, 5399–5413. [CrossRef]
24. Qiu, Y.; Xie, Z.; Kang, P.; Chen, P.; Fang, Y. Polar-coded Gaussian Multiple-Access Channels with Physical-Layer Network Coding. *IEEE Trans. Veh. Technol.* **2024**, 1–6.. [CrossRef]
25. Pan, Y.; Wang, K.; Pan, C.; Zhu, H.; Wang, J. UAV-Assisted and Intelligent Reflecting Surfaces-Supported Terahertz Communications. *IEEE Wirel. Commun. Lett.* **2021**, *10*, 1256–1260. [CrossRef]
26. Misbah, M.; Kaleem, Z.; Khalid, W.; Yuen, C.; Jamalipour, A. Phase and 3-D Placement Optimization for Rate Enhancement in RIS-Assisted UAV Networks. *IEEE Wirel. Commun. Lett.* **2023**, *12*, 1135–1138. [CrossRef]
27. Ranjha, A.; Kaddoum, G. URLLC Facilitated by Mobile UAV Relay and RIS: A Joint Design of Passive Beamforming, Blocklength, and UAV Positioning. *IEEE Internet Things J.* **2021**, *8*, 4618–4627. [CrossRef]
28. Li, S.; Duo, B.; Renzo, M.D.; Tao, M.; Yuan, X. Robust Secure UAV Communications with the Aid of Reconfigurable Intelligent Surfaces. *IEEE Trans. Wirel. Commun.* **2021**, *20*, 6402–6417. [CrossRef]
29. Nguyen, N.T.; Nguyen, V.D.; Van Nguyen, H.; Wu, Q.; Tölli, A.; Chatzinotas, S.; Juntti, M. Fairness Enhancement of UAV Systems with Hybrid Active-Passive RIS. *IEEE Trans. Wirel. Commun.* **2023**, 1. [CrossRef]
30. Zhi, K.; Pan, C.; Ren, H.; Chai, K.K.; Elkashlan, M. Active RIS Versus Passive RIS: Which is Superior with the Same Power Budget? *IEEE Commun. Lett.* **2022**, *26*, 1150–1154. [CrossRef]
31. Thantharate, P.; Thantharate, A.; Kulkarni, A. GREENSKY: A fair energy-aware optimization model for UAVs in next-generation wireless networks. *Green Energy Intell. Transp.* **2024**, *3*, 100130. [CrossRef]
32. Adam, A.B.M.; Ouamri, M.A.; Wan, X.; Muthanna, M.S.A.; Alkanhel, R.; Muthanna, A.; Li, X. Secure Communication in UAV–RIS-Empowered Multiuser Networks: Joint Beamforming, Phase Shift, and UAV Trajectory Optimization. *IEEE Syst. J.* **2024**, 1–11. [CrossRef]
33. Lv, W.; Bai, J.; Yan, Q.; Wang, H.M. RIS-Assisted Green Secure Communications: Active RIS or Passive RIS? *IEEE Wirel. Commun. Lett.* **2023**, *12*, 237–241. [CrossRef]
34. Zhang, Z.; Dai, L.; Chen, X.; Liu, C.; Yang, F.; Schober, R.; Poor, H.V. Active RIS vs. Passive RIS: Which Will Prevail in 6G? *IEEE Trans. Commun.* **2023**, *71*, 1707–1725. [CrossRef]
35. Di Renzo, M.; Debbah, M.; Phan-Huy, D.T.; Zappone, A.; Alouini, M.S.; Yuen, C.; Sciancalepore, V.; Alexandropoulos, G.C.; Hoydis, J.; Gacanin, H.; et al. Smart Radio Environments Empowered by AI Reconfigurable Meta-Surfaces: An Idea Whose Time Has Come. *EURASIP J. Wirel. Commun. Netw.* **2019**, *2019*, 129. [CrossRef]
36. Ozdogan, O.; Bjornson, E.; Larsson, E.G. Intelligent Reflecting Surfaces: Physics, Propagation, and Pathloss Modeling. *IEEE Wirel. Commun. Lett.* **2020**, *9*, 581–585. [CrossRef]

37. Nadeem, Q.U.A.; Kammoun, A.; Chaaban, A.; Debbah, M.; Alouini, M.S. Asymptotic Max-Min SINR Analysis of Reconfigurable Intelligent Surface Assisted MISO Systems. *IEEE Trans. Wirel. Commun.* **2020**, *19*, 7748–7764. [CrossRef]
38. Bjornson, E.; Ozdogan, O.; Larsson, E.G. Intelligent Reflecting Surface Versus Decode-and-Forward: How Large Surfaces are Needed to Beat Relaying? *IEEE Wirel. Commun. Lett.* **2020**, *9*, 244–248. [CrossRef]
39. Nadeem, Q.U.A.; Kammoun, A.; Debbah, M.; Alouini, M.S. A Generalized Spatial Correlation Model for 3D MIMO Channels Based on the Fourier Coefficients of Power Spectrums. *IEEE Trans. Signal Process.* **2015**, *63*, 3671–3686. [CrossRef]
40. Yu, H.; Tuan, H.D.; Duong, T.Q.; Poor, H.V.; Fang, Y. Optimization for Signal Transmission and Reception in a Macrocell of Heterogeneous Uplinks and Downlinks. *IEEE Trans. Commun.* **2020**, *68*, 7054–7067. [CrossRef]
41. Tam, H.H.M.; Tuan, H.D.; Ngo, D.T. Successive Convex Quadratic Programming for Quality-of-Service Management in Full-Duplex MU-MIMO Multicell Networks. *IEEE Trans. Commun.* **2016**, *64*, 2340–2353. [CrossRef]